

PAPER

Neoclassical flows in deuterium–helium plasma density pedestals

To cite this article: S Buller *et al* 2017 *Plasma Phys. Control. Fusion* **59** 055019

View the [article online](#) for updates and enhancements.

Related content

- [Isotope and density profile effects on pedestal neoclassical transport](#)
S Buller and I Pusztai
- [Global effects on neoclassical transport in the pedestal with impurities](#)
I Pusztai, S Buller and M Landreman
- [Radially global f computation of neoclassical phenomena in a tokamak pedestal](#)
Matt Landreman, Felix I Parra, Peter J Catto et al.

Recent citations

- [Isotope and density profile effects on pedestal neoclassical transport](#)
S Buller and I Pusztai

Neoclassical flows in deuterium–helium plasma density pedestals

S Buller¹, I Pusztai¹, S L Newton^{1,2} and J T Omotani¹

¹Department of Physics, Chalmers University of Technology, SE-41296 Göteborg, Sweden

²CCFE, Culham Science Centre, Abingdon, Oxon OX14 3DB, United Kingdom

E-mail: bstefan@chalmers.se

Received 24 November 2016, revised 15 February 2017

Accepted for publication 9 March 2017

Published 5 April 2017



Abstract

In tokamak transport barriers, the radial scale of profile variations can be comparable to a typical ion orbit width, which makes the coupling of the distribution function across flux surfaces important in the collisional dynamics. We use the radially global steady-state neoclassical δf code PERFECT (Landreman *et al* 2014 *Plasma Phys. Control. Fusion* **56** 045005) to calculate poloidal and toroidal flows, and radial fluxes, in the pedestal. In particular, we have studied the changes in these quantities as the plasma composition is changed from a deuterium bulk species with a helium impurity to a helium bulk with a deuterium impurity, under specific profile similarity assumptions. In the presence of sharp profile variations, the poloidally resolved radial fluxes are important for the total fluxes to be divergence-free, which leads to the appearance of poloidal return-flows. These flows exhibit a complex radial–poloidal structure that extends several orbit widths into the core and is sensitive to abrupt radial changes in the ion temperature gradient. We find that a sizable neoclassical toroidal angular momentum transport can arise in the radially global theory, in contrast to the local.

Keywords: neoclassical transport, tokamak, radially global, pedestal, flows, deuterium, helium

(Some figures may appear in colour only in the online journal)

1. Introduction

Transport barriers are regions in a magnetically confined plasma with reduced cross-field turbulent transport, which leads to steep gradients in density and temperature. Such formations have a major impact on fusion plasmas, as they can enable fusion relevant conditions to be reached in smaller devices. Thus, practically all plans for future magnetic fusion experiments and reactors include at least an edge transport barrier, commonly known as *the pedestal*.

Since the discovery of transport barriers (the ELMy H-mode [1]) there have been numerous studies [2–6] indicating the crucial role plasma flows play in the transition to improved confinement regimes. In particular, the equilibrium flows have been experimentally observed to play a major role in setting the transition threshold [7]. Thus well resolved plasma flow measurements in the pedestal, especially those of the main ion species, are highly desirable for progress in the understanding of the barrier formation.

However, the flows of fusion relevant hydrogen ions are challenging to infer directly due to their involved emission spectrum, which complicates the use of standard charge exchange techniques (see [8] for a recent effort to tackle these difficulties in DIII-D). Instead, flow diagnostics often rely on measuring the flows of some impurity species, such as He [9], B [10] and C [9, 11], from which the deuterium flows are inferred. Yet another technique is to measure the main ion flows in non-hydrogenic plasmas; this approach has been used with helium plasmas, in DIII-D [12], and recently in ASDEX Upgrade [13].

That being said, theoretical calculations are required to relate these flows to deuterium flows. Specifically, it is important to know how impurity ion flows relate to main ion flows, and how the flows in helium and deuterium bulk plasmas compare to each other. These questions have previously been addressed with local neoclassical predictions [14, 15]. Such local calculations assume a scale separation between the radial variations in plasma profiles and the orbit width, thus they are not necessarily applicable to the H-mode

pedestal, where profiles can vary significantly over an orbit width. It is in the pedestal where flow measurements would be particularly interesting in order to study the H-mode, and neoclassical effects may be expected to contribute most strongly as a result of the reduced turbulent transport.

To address these questions in relation to the pedestal, we numerically investigate neoclassical flows in deuterium and helium plasmas, using the neoclassical global δf code PERFECT (pedestal and edge radially-global Fokker–Planck evaluation of collisional transport) [16, 17]. The model profiles used here follow the approach of [18] to capture features of experimental JET pedestals [19] in multi-species simulations, while remaining within the validity of the δf theory.

Due to the radial coupling in the global theory, the resulting fluxes are not divergence free within flux-surfaces. Thus flows within flux surfaces should be considered together with the radial flows. This has been considered as an explanation for poloidal impurity flow observations in [20], although modeling of the radial–poloidal flow structures was outside the scope of their study. In this paper, we discuss radial transport alongside poloidal and toroidal flows.

In section 2, we describe the radially global δf theory, including constraints posed by our linearization about a Maxwell–Boltzmann distribution. In section 3, we relate the assumptions presented in the previous section to design choices in our numerical study, and present two bulk helium scenarios based on different similarity assumptions. Flows in both local and global simulations are presented, and we find that the global poloidal flows display notably larger poloidal and radial variations, with odd-parity in–out structure, which is sensitive to changes in the temperature gradient. Poloidally resolved radial flows are then considered together with poloidal flows. Finally, we consider the total radial transport of particles, heat and toroidal angular momentum. In global simulations we observe order unity modifications to the local particle and heat fluxes, both inside the pedestal and a few orbit widths into the core. More importantly the angular momentum flux can become significant in the global simulations.

2. Global δf drift-kinetics

Assuming that there is a sufficient scale separation between the gyroradius and the background profiles, and excluding fast transients, collisional transport can be calculated from the drift-kinetic equation (DKE)

$$\frac{\partial f}{\partial t} + (v_{\parallel} \mathbf{b} + \mathbf{v}_d) \cdot \nabla f = C[f]. \quad (1)$$

The terms in the above equation are: f , the gyroaveraged distribution function; $v_{\parallel} = \mathbf{v} \cdot \mathbf{b}$, with \mathbf{v} the velocity, $\mathbf{b} \equiv \mathbf{B}/B$, with \mathbf{B} the magnetic field and $B \equiv |\mathbf{B}|$; the drift velocity \mathbf{v}_d —which we decompose into $E \times B$ and magnetic drifts $\mathbf{v}_d = \mathbf{v}_E + \mathbf{v}_m$, $\mathbf{v}_E = B^{-2} \mathbf{E} \times \mathbf{B}$, $\mathbf{v}_m = v_{\parallel}^2 \Omega^{-1} \nabla \times \mathbf{b} + v_{\perp}^2 (2\Omega B^2)^{-1} \mathbf{B} \times \nabla B$, $\Omega = ZeB/m$; is the gyrofrequency,

with e the elementary charge, Ze the species charge; $\mathbf{v}_{\perp} = \mathbf{v} - v_{\parallel} \mathbf{b}$ is the velocity perpendicular to \mathbf{b} . C is a collision operator—here the Fokker–Planck operator. The gradients are taken with total energy $W = mv^2/2 + Ze\Phi$ and magnetic moment $\mu = mv_{\perp}^2/(2B)$ held constant, where Φ is the electrostatic potential.

To obtain a linear theory, we expand the distribution function f around a flux function, stationary Maxwell–Boltzmann distribution $f_M(\psi)$, $f = f_M + f_1 + \mathcal{O}(\delta^2 f_M)$, $f_1/f_M = \mathcal{O}(\delta)$. Here $2\pi\psi$ is the poloidal magnetic flux, which we use as our flux-surface label; δ is an expansion parameter representing the smallness of the thermal ion orbit width compared to the scale of the device, to be defined more rigorously once we derive further validity conditions for the linearization. In general, a physical quantity X is decomposed as $X = X_0 + X_1$. From the decomposition of the distribution function, it follows that the zeroth order density n_0 and temperature T_0 profiles are flux functions; and that the total flow velocities in the laboratory frame are much smaller than the thermal speed of the species (i.e. ‘low-flow ordering’). In addition, we assume $\Phi_0 = \Phi_0(\psi)$. These assumptions are made for the sake of convenience, and do not represent an inherent limitation of the δf framework³.

Defining the non-adiabatic part of f_1 as

$$g = f_1 - \frac{Ze\Phi_1}{T} f_M, \quad (2)$$

we linearize (1) to obtain

$$(v_{\parallel} \mathbf{b} + \mathbf{v}_{d0}) \cdot (\nabla g)_{W_0, \mu} - C_1[g] = -v_m \cdot (\nabla f_M)_{W_0, \mu}, \quad (3)$$

where C_1 is the linearized Fokker–Planck operator, $W_0 = mv^2/2 + Ze\Phi_0$; Φ_1 has been eliminated from the drift velocity $\mathbf{v}_{d0} = B^{-2} \mathbf{B} \times \nabla \Phi_0 + \mathbf{v}_m$ and we have assumed a steady state distribution, $\partial f / \partial t = 0$.

We are now in a position to more precisely define our expansion parameter δ . By construction, $g/f_M = \mathcal{O}(\delta)$, thus δ measures the size of g . The size of g scales with the inhomogeneous term on the right-hand side of (3), which can be approximated as [17]

$$v_m \cdot (\nabla f_M)_{W_0, \mu} = v_m \cdot \nabla \psi \frac{\partial}{\partial \psi} \bigg|_{W_0} \left[\left(\frac{m}{2\pi T_0} \right)^{3/2} \eta_0 e^{\frac{W_0}{T_0}} \right], \quad (4)$$

where W_0 is a constant with respect to our derivative, and we have introduced the *pseudo-density*

$$\eta_0(\psi) = n_0 e^{Ze\Phi_0/T_0}. \quad (5)$$

(Henceforth, to streamline notation, the subscript ‘0’ will be dropped.) It follows from (4) that only the temperature and η gradients enter into the inhomogeneous term in (3) and thus set the size of g and act to make the distribution function non-Maxwellian. To characterize the size of the gradients of a

³ One possible generalization is to include order unity density variations on a flux surface, which naturally develop for impurities in the pedestal [21–25]. Such poloidal variations have been implemented in the stellarator code SFNCS [26, 27] that shares a very similar numerical framework to PERFECT.

plasma parameter X we introduce

$$\delta_X \equiv \frac{\rho_p}{L_X}, \quad (6)$$

where $\rho_p = mv_T/(ZeB_p)$ is the poloidal gyroradius, with the poloidal magnetic field B_p , and thermal velocity $v_T = \sqrt{2T/m}$; and $L_X = -[d(\ln X)/dr]^{-1}$ is the scale length of X . Since the size of the departure from f_M depends on the gradients in η and T , we can finally give a conservative definition of our expansion parameter δ as

$$\delta = \max_{\psi: X=\eta_a, T_a} \delta_X(\psi) \ll 1, \quad (7)$$

where a is a species index. In words, δ is the largest value of the δ_X profiles corresponding to $T_a(\psi)$ and $\eta_a(\psi)$, among all species.

Note that while n and Φ can vary on shorter length scales if the corresponding η has a slow radial variation, the DKE (1) itself is based on an expansion in $\rho/L_X = (B_p/B)\delta$ for all plasma parameters, so no plasma profile may have gyroradius scale variation. We also require $B_p/B \ll 1$ to ensure that the gyroradius and the orbit-width expansions can be performed separately.

Equation (3) is the global linearized DKE, from which the conventional local δf equation can be recovered by dropping the $\mathbf{v}_{d0} \cdot \nabla g$ term. The latter is solved when we refer to ‘local’ solutions. This corresponds to ordering $\nabla g = \mathcal{O}(\delta f_M/L)$, meaning that the radial variation of g —and thus the radial variation of radial fluxes [16]—appear at order $(B_p/B)\delta^2 n v_T/L$ in (3). Note that neglecting $\mathbf{v}_m \cdot \nabla g$ means that ψ only appears as a parameter in the local equation, while the global equation is a differential equation in ψ , and thus requires radial boundary conditions. (In this work, we use solutions to the local equation as boundary conditions; see the first part of section 3 for details.)

In the pedestal region, $\mathbf{v}_{d0} \cdot \nabla g$ must be retained, as the *radial variation* of the fluxes is in general not small in the presence of sharp background profiles. However, radially varying steady-state particle fluxes are inconsistent with particle conservation, unless they are compensated for by sources in the DKE (3) [16].

These sources may represent real sources, due to atomic physics processes, but could also include the radial variation of other fluxes—due to e.g. turbulence—which are excluded from our modeling but needed to cancel the radial variation of the modeled fluxes. We thus add a source term S to (3) and obtain

$$(\mathbf{v}_{\parallel} \mathbf{b} + \mathbf{v}_{d0}) \cdot (\nabla g)_{W,\mu} - C_1[g] = -\mathbf{v}_m \cdot (\nabla f_M)_{W,\mu} + S, \quad (8)$$

which is the equation we solve when we refer to ‘global’ solutions.

The velocity and poloidal dependence of the sources are specified to yield particle and heat sources, while the radial dependence of these sources is solved for alongside g by imposing that the perturbed distribution function should have zero flux-surface averaged density and pressure. This means that the input profiles specify the flux surface averages, that is

$$X_0 = \langle X \rangle \equiv (V')^{-1} \oint X |\mathbf{B} \cdot \nabla \theta|^{-1} d\theta, \quad (9)$$

$$V' \equiv \oint |\mathbf{B} \cdot \nabla \theta|^{-1} d\theta, \quad (10)$$

where θ is an angle-like poloidal coordinate, and we introduced the flux surface average, denoted by $\langle \cdot \rangle$. In this work, we assume that the sources have no poloidal dependence, and have the same velocity structure as in [17].

3. Simulations and results

We consider a plasma with deuterium as bulk species and helium as impurity, and a bulk helium plasma with a deuterium impurity species, as two extreme cases of an ion concentration scan.

We would like to focus on differences in neoclassical phenomena that are linked to the charge and mass of the various ion components; our philosophy is thus to minimize changes in the plasma profiles as the ion composition is changed. In reality, plasma with different ion composition can have significantly different profiles, for reasons ranging from basic physical differences related to mass and charge dependences of various phenomena [28] to more practical ones, such as differences in heating or recycling [29].

Forgoing these complications, we consider two scenarios, with profiles based on different similarity assumptions, which we refer to as *fixed* Φ and *fixed* n_e . The different names indicate which profile in the quasi-neutrality condition,

$$n_e = Z_D \eta_D e^{-Z_D e \Phi / T_D} + Z_{He} \eta_{He} e^{-Z_{He} e \Phi / T_{He}}, \quad (11)$$

is kept fixed when changing from a D to He bulk plasma. It is convenient to express this relation in terms of the ion pseudo-densities and temperatures, as these are constrained by (7).

For the ion pseudo-density profiles we use linear profiles, with a slope based on the experimental JET outer core n_e profile of figure 16 in [19]; these core gradients generally satisfy the constraints posed by (7). Likewise, our ion temperature profiles were based on the core temperature gradient of the same figure. In addition, we further reduce the ion temperature gradients in the core to make a proxy for the local deuterium heat flux, $Q_D \sim n_D T_D^{3/2} \partial_\psi T_D$, equal at the boundaries. This change in gradients both reduces the total heat and particle sources, when integrated over the simulation domain, while it also leads to a localization of sources around the pedestal region [17]. We will discuss the effect of changes in the temperature gradient in section 3.1.1.

The electron temperature profile is allowed to have structure on the ion orbit width scale, and thus uses the full temperature profile in figure 16 of [19]. We note that, as a consequence, the electron flows are much larger than the ion flows in absolute magnitude, and thus the bootstrap current is dominated by the electron contribution. As a result, the fixed n_e similarity class keeps the bootstrap current profile practically fixed.

In the fixed Φ scenario, Φ is then chosen to make n_D similar to the experimental n_e profile. Finally, n_{He} is determined by Φ , T_{He} and η_{He} . Bulk D and He plasmas are

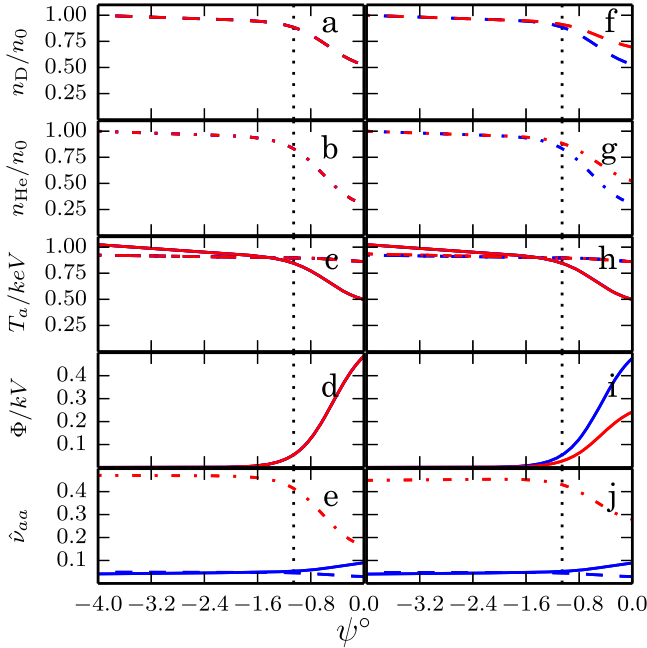


Figure 1. Input profiles (a)–(d), (f)–(i) used in the fixed Φ scan (left column) and fixed n_e scan (right column), and the collisionality (e), (j) for the different species in the simulations in which their density is highest. Solid: electrons, dashed: deuterium, dash-dotted: helium. Bulk species is deuterium (blue curves), or helium (red curves), note that the curves overlap.

obtained by rescaling the ion η profiles relative to each other, which yields electron density profiles that vary with the ion concentrations—while leaving δ_η unaffected. Although the shape of n_e varies, the ion profiles are re-scaled to yield the same electron density at the pedestal top.

In the fixed n_e scenario, n_e is instead specified from the experimental n_e profile, and Φ is obtained from the quasi-neutrality condition (11), and thus depends on the helium concentration. Note that for a pure deuterium plasma, the methods yield the same Φ , and thus the bulk deuterium simulations are approximately the same in both similarity classes.

The pedestal usually extends outside the last closed flux surface (LCFS), while our model is restricted to closed field lines. We consider the region which would be in the open field line region as a numerical buffer region of the simulation. Such a region is introduced to better accommodate the outer radial boundary condition imposed in the simulation: a solution to the *local* DKE is imposed as boundary condition where particles enter the radial domain. For the local DKE to be valid, the density profiles in the buffer region have artificially reduced, core relevant, gradients. Since the results in the buffer region are not necessarily physically meaningful, we do not show this region in the figures.

The resulting input profiles are depicted in figure 1, for the fixed Φ and fixed n_e scan (left and right columns, respectively). In both scans the blue profiles are for bulk-deuterium plasmas ($n_{\text{He}}/n_{\text{D}} = 0.01$ in the core region) and red lines are for bulk-helium plasmas ($n_{\text{D}}/n_{\text{He}} = 0.01$); solid lines are electron profiles, dashed lines are deuterium and

dash-dotted lines helium. As a radial coordinate we use

$$\psi^\circ = \frac{\psi - \psi_{\text{LCFS}}}{\left\langle \frac{1}{B_p} \frac{\partial \psi}{\partial r} \right\rangle \sqrt{\epsilon T_{\text{D}} m_{\text{D}} / e}}, \quad (12)$$

which is the poloidal flux normalized and shifted so that $\psi^\circ = 0$ at the LCFS and a unit change of ψ° corresponds to a typical trapped thermal deuterium orbit width at ψ ; ϵ is the inverse aspect ratio (defined as in Miller geometry [30]). The last subfigures in figure 1 depict the species self-collisionalities

$$\hat{\nu}_{aa} = \frac{\nu_{aa}}{v_{\text{T}}/qR_0} = \frac{qR_0}{12\pi^{3/2}} \frac{Z_a^4 e^4 n_a \ln \Lambda}{\epsilon_0^2 T_a^2}, \quad (13)$$

in the simulations that yield the highest collisionality for the specific species: $\hat{\nu}_{\text{DD}}$ and $\hat{\nu}_{\text{ee}}$ are given for the bulk D plasma, and $\hat{\nu}_{\text{HeHe}}$ is given for bulk He. Here, q is the safety factor, R_0 the major radius at the magnetic axis, and ν_{aa} the self-collision frequency of species a [31]. Since $\hat{\nu}_{aa} \ll 1$, all our simulations have all species in the banana regime—with the bulk helium plasma being an exception, where $\hat{\nu}_{\text{HeHe}} \approx 0.5$.

In the following figures, curves are color coded as in figure 1 to indicate ion composition. In addition, dashed lines indicate output from local simulations, and solid lines are global results. The same color and line styles are applied to the frames of 2D plots. The following normalization is used throughout the paper. Quantities with a hat are normalized to a reference quantity that is species-independent in most cases, $\hat{X} = X/\bar{X}$. The reference quantities used in this work are: $\bar{R} = 3.8$ m, $\bar{B} = 2.9$ T, $\bar{n} = 10^{20}$ m $^{-3}$, $\bar{T} = e\bar{\Phi} = 1$ keV, $\bar{m} = m_{\text{D}}$, where m_{D} is the deuterium mass. These numbers are based on ‘typical’ quantities for JET, and only affect the normalization of the results. From these, we define a reference speed as $\bar{v} = \sqrt{2\bar{T}/\bar{m}}$, and the dimensionless constant $\Delta = \bar{m}\bar{v}/(\bar{e}\bar{B}\bar{R})$, which corresponds to a normalized gyroradius at the reference quantities. Specifically, we have: fluid flow velocity $\hat{V} = V/(\Delta\bar{v})$; sources $\hat{S}_a = \bar{v}^2 \bar{R} S_a / (\Delta \bar{n} \hat{m}_a^{3/2})$; flux surface incremental volume $\hat{V}' = (\bar{B}/\bar{R}) d_\psi V$, particle flux, $\hat{\Gamma}_a = \int d^3v g_a v_{\text{ma}} / (\bar{n}\bar{v})$; toroidal momentum flux (divided by mass), $\hat{\Pi}_a = \int d^3v g_a v_{\parallel} I v_{\text{ma}} / (\bar{n}\bar{v}^2 \bar{R} B)$, with $I(\psi) = RB_t$, R the major radius and B_t the toroidal magnetic field; heat flux, $\hat{Q}_a = \int d^3v g_a m_a v^2 v_{\text{ma}} / (2\bar{T}\bar{n}\bar{v})$; conductive heat flux, $\hat{q}_a = \hat{Q}_a - (5/2)\bar{T}\hat{\Gamma}_a$. In addition, we define the normalized scalar radial particle flux

$$\hat{\Gamma}_a = \frac{\hat{V}'}{\Delta^2 \pi \bar{R} \bar{B}} \langle \hat{\Gamma}_a \cdot \nabla \psi \rangle \quad (14)$$

and analogously, scalar fluxes for heat and momentum. When comparing poloidal and radial fluxes (as in figure 6), it is convenient to instead project the radial fluxes on a unit vector, in which case we use $\hat{\Gamma}_a \cdot \psi$, with $\psi = \nabla \psi / (RB_p)$ being the unit vector in the $\nabla \psi$ -direction.

3.1. Flows

First we study the radial and poloidal structure of the particle flows. As we will see, the flows in global simulations exhibit

qualitatively different features from the local results. In local theory the flows should be divergence-free on each flux surface in isolation. This is broken in the global case where radial flows play an important role in making the total flow divergence-free. Before discussing the flows in the fixed Φ and fixed n_e similarity classes, we express the toroidal and poloidal flows, V_t and V_p , in terms of g ,

$$V_p = \frac{B_p}{nB} \int d^3v v_{\parallel} g + \frac{T}{mB\Omega} IB_p \left[\frac{p'}{p} + \frac{Ze\Phi'}{T} \right] + \frac{IB_p}{nB^2} \Phi' \int d^3v g + \frac{IB_p}{2nB\Omega} \frac{\partial}{\partial \psi} \int d^3v v_{\perp}^2 g, \quad (15)$$

$$V_t = \frac{B_t}{nB} \int d^3v v_{\parallel} g - \frac{T}{mB\Omega} B_p^2 R \left[\frac{p'}{p} + \frac{Ze\Phi'}{T} \right] - \frac{B_p^2 R}{nB^2} \Phi' \int d^3v g - \frac{B_p^2 R}{2nB\Omega} \frac{\partial}{\partial \psi} \int d^3v v_{\perp}^2 g, \quad (16)$$

where a prime denotes a ψ derivative and $p = nT$. The above expressions are accurate to first order in $\delta B_p/B$, and thus include corrections due to the gyrophase dependent part of the distribution function $\tilde{f} \approx -\rho \cdot \nabla f$, where $\rho = \Omega^{-1} \mathbf{b} \times \mathbf{v}_{\perp}$ is the gyroradius vector. In the global theory, \tilde{f} contributes with a $-\rho \cdot \nabla g$ term, which gives the additional corrections to the diamagnetic and $E \times B$ flows on the second rows of the above equations. Equation (15) was calculated in [16] (note that g in [16] is defined differently), and (16) is calculated analogously. We note, that while all terms are comparable in (15), the global corrections to V_t are small in B_p/B compared to the usual expression (the first line of (16)); nevertheless, we keep them for completeness.

Since all the terms in V_p are proportional to B_p/B , we factor out this trivial poloidal dependence and define the *poloidal flow coefficient*

$$k_p = \frac{Ze \langle B^2 \rangle}{IB_p} \left(\frac{dT_0}{d\psi} \right)^{-1} V_p, \quad (17)$$

which reduces to the conventional flux function *parallel flow coefficient* in the local limit [16] (assuming the lowest order distribution to be a flux function).

3.1.1. Fixed Φ profile flows. Using (15)–(17) and the fixed Φ input profiles in figure 1, we obtain the ion flows, k_p and \hat{V}_t , displayed in figure 2.

For the toroidal flows—even though the terms in the second line of (16) are negligible—global effects have an impact through the modifications to g . Comparing the global toroidal flow results, figures 2(a), (b), (e) and (f), to the corresponding local ones, figures 2(c), (d), (g) and (h), the most striking difference is that close to the LCFS the toroidal flow changes sign at the high-field side (HFS, $\theta = \pi$). As a general trend seen at all poloidal locations the global toroidal flows are elevated in the core plasma, and reduced in the pedestal.

The poloidal flow coefficients are flux functions in the local case, as seen in figures 2(k), (l), (o) and (p). However, the corresponding global results exhibit complex radial–

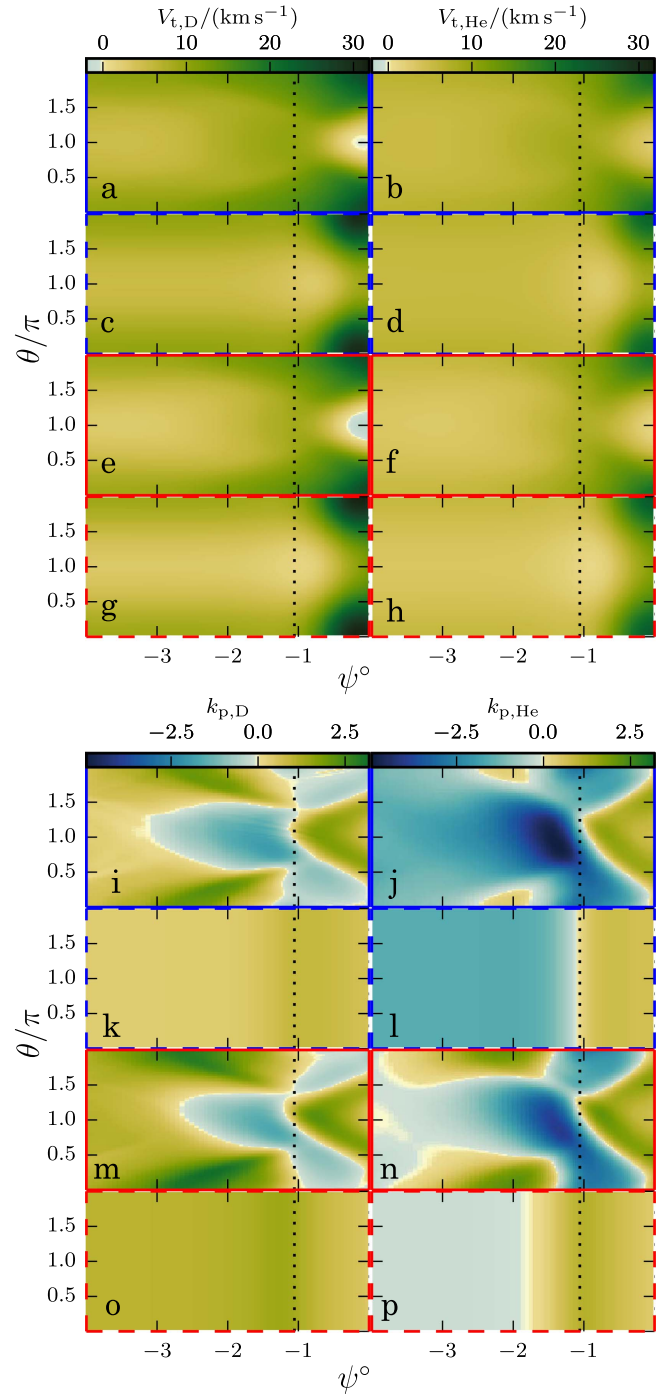


Figure 2. D and He toroidal flows (a)–(h) and poloidal flow coefficients (i)–(p) for bulk deuterium ((a)–(d), (i)–(l), blue) and bulk helium ((e)–(h), (m)–(p), red) plasmas, in the fixed Φ scan. Dashed frames (c)–(d), (g)–(h), (k)–(l), (o)–(p) are local results.

poloidal features, shown in figures 2(i), (j), (m) and (n). In particular, significant poloidal variations appear in the flows, that include sign changes.

The high field side (HFS, $\theta = \pi$, thick lines) and low field side (LFS, $\theta = 0$, thin lines) toroidal and poloidal flows are shown in figures 3(a)–(c) and (d)–(f), respectively. The electron flows are mostly local due to their small orbit width and our low flow ordering. However, for ions, changing from

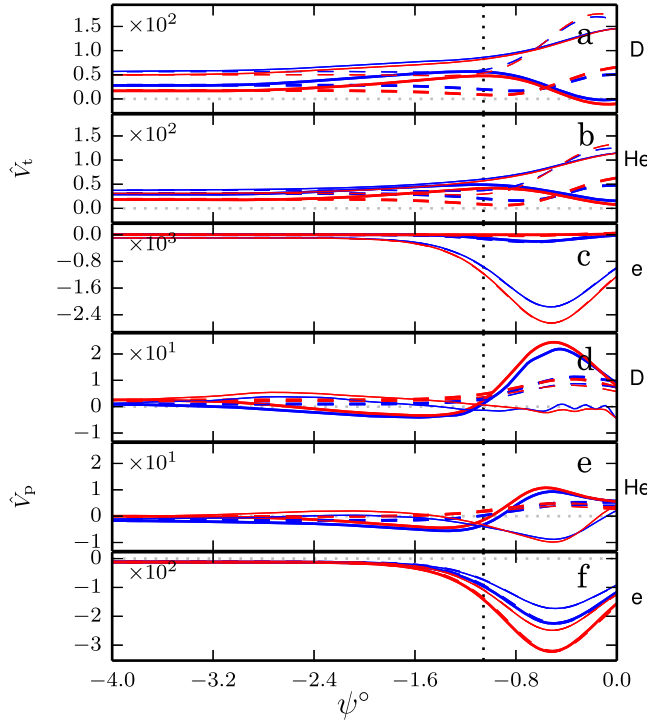


Figure 3. Toroidal (a)–(c) and poloidal (d)–(f) flows at the LFS ($\theta = 0$, thin lines) and HFS (thick, $\theta = \pi$), in the fixed Φ scan. Main species is deuterium (blue lines) or helium (red). Solid (dashed) lines correspond to global (local) results.

local (dashed lines) to global (solid lines) simulations leads to important changes. For instance, in the global case, while the LFS toroidal flows monotonically increase for both ion species throughout radial range plotted, their HFS counterparts decrease in the pedestal, and even change sign for deuterium. On the other hand, for a given ion species, the effects of changing its role from bulk to impurity are rather small, and they are similar in the global and local simulations (blue curves: D bulk; red: He bulk). In the weakly collisional limit of the local theory, even those flow contributions, which are ultimately caused by collisions, become independent of collision frequency. The observed weak variation with changing ion concentration seen here is the result of these cases not being asymptotically collisionless and due to inter-species coupling (as confirmed by simulations with artificially increased collisionality, not shown here). This feature remains valid in the global case as well.

3.1.2. Fixed n_e profile flows. In contrast to the fixed Φ scenario, in the fixed n_e scenario both Φ and the ion density profiles change with ion composition, which is expected to be reflected in the ion flows. Since these profile changes are limited to the pedestal region, this is where corresponding effects are expected in the local theory. All modifications to local flows outside the pedestal are the result of changes in collisionality, and thus should be similar in the two similarity classes. In the global theory the effect of the changes in the pedestal profiles will propagate outside the pedestal due to the radial coupling of g . It is important that, although in the pedestal Φ and the ion density gradients

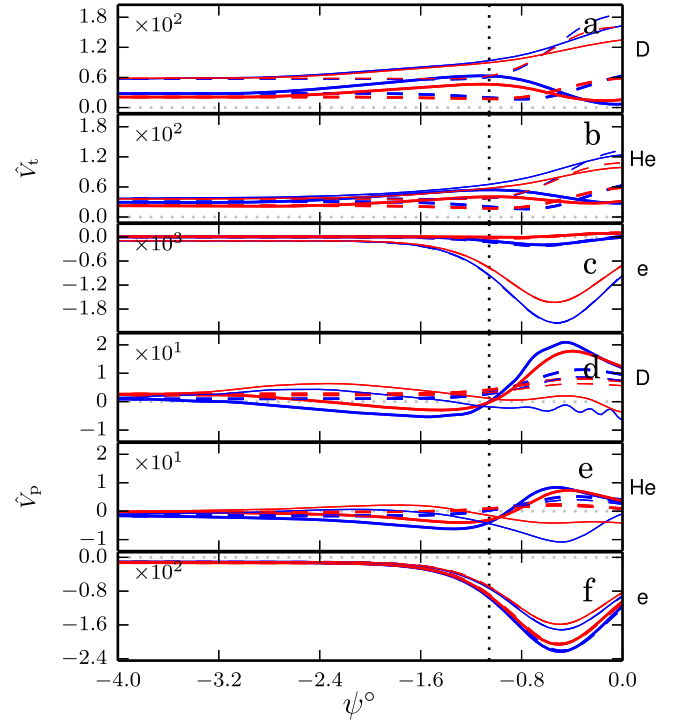


Figure 4. Toroidal (a)–(c) and poloidal (d)–(f) flows at the LFS ($\theta = 0$, thin lines) and HFS (thick, $\theta = \pi$), in the fixed n_e scan. Main species is deuterium (blue lines) or helium (red). Solid (dashed) lines correspond to global (local) results.

change in the scan, the η gradient is not changed due to the construction of our model profiles. This means that any differences observed are not due to changes in $\partial_\psi f_M$, but due to changes in the finite orbit width effects (the magnitude of the radial electric field is reduced with increasing He concentration).

The flows depicted in figures 4 and 5 do not reveal a striking variation with plasma composition. If we compare the LFS ion flows in the pedestal (thin lines, sub-figures: (a) and (b), (d) and (e); at $\psi^o = 0$) in figure 4 to the corresponding fixed Φ figure, figure 3, we indeed see a stronger effect of exchanging bulk and impurity species, although the two different scans produce curves with the same qualitative features. On the other hand, the HFS flows are not affected as strongly. Overall, the effect of changing the helium concentration is small in both scans. Thus, for our low collisionality, slight variations in density profiles do not matter much. The similarities between the two scans can also be verified by looking at the full poloidal dependence of the flows, shown in figure 5 for the bulk helium simulation.

Since we have established that the electron dynamics is not too much affected by our low-flow ordered ions, and the n_e profile is held fixed, we expect the poloidal electron dynamics to exhibit only a modest change in the scan. Comparing the differences between the bulk D (blue) and bulk He (red) curves in between figures 4(f) and 3(f), we find that this is indeed the case. On the other hand, the toroidal flow of electrons changes in the fixed n_e scan, as the radial electric field varies with ion composition.

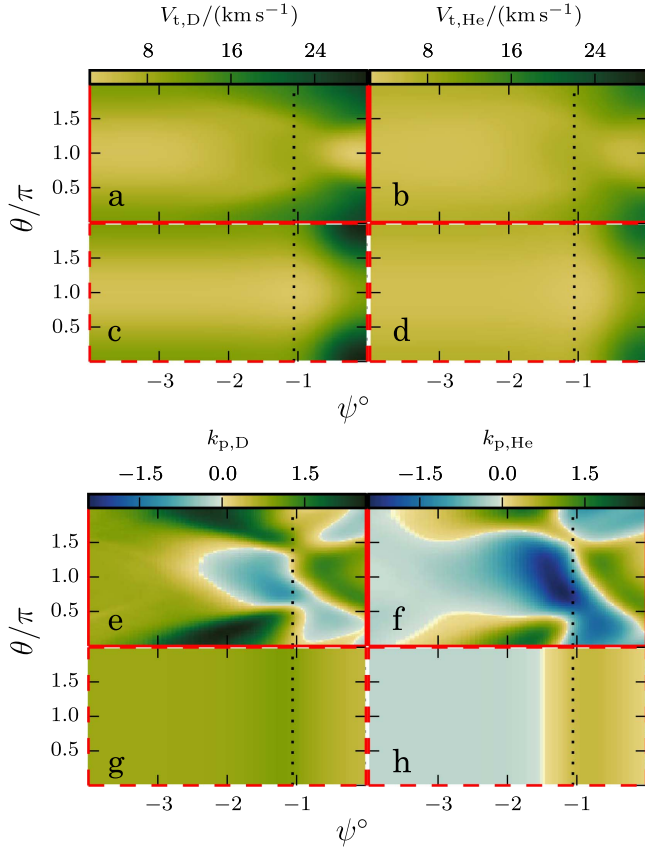


Figure 5. Toroidal flows (a)–(d) and poloidal flow coefficients (e)–(h) in a bulk helium plasma similar to figures 2(e)–(h) and (m)–(p), but for fixed n_e profiles.

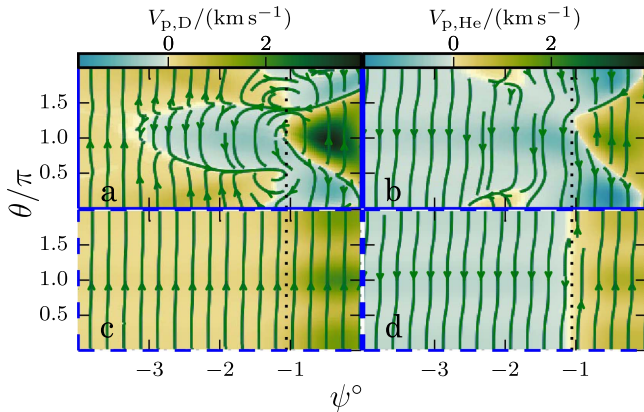


Figure 6. A stream-plot of fluxes in the radial-poloidal plane, overlaid on a color map of the poloidal flows, in a bulk deuterium plasma. Deuterium (a)–(c) and helium (b)–(d) species in global (a), (b) and local (c), (d) simulations.

3.1.3. Interplay of the poloidal and radial dynamics. In the global simulations we found that the poloidal flow can change sign between different poloidal locations. This is possible because the divergence of the radial flux can make the total radial-poloidal fluxes divergence free. (We use the term ‘flux’ instead of ‘flow’, because the radial variation of the density is not negligible in our simulations.) It is therefore instructive to consider the full radial-poloidal structure of the fluxes. Figure 6 shows a stream plot of the fluxes in the poloidal and

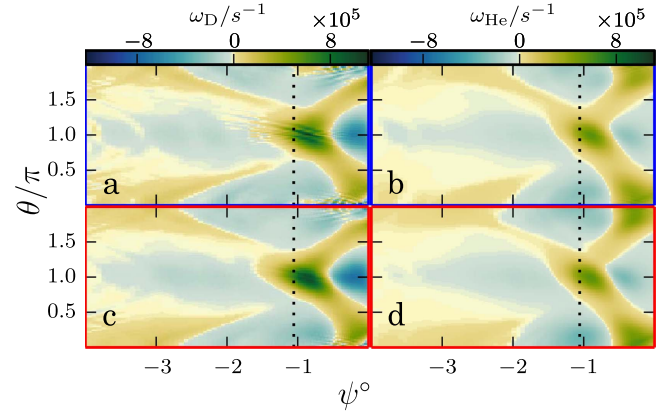


Figure 7. Deuterium and helium vorticity (defined in (18)) for bulk deuterium ((a)–(b), blue) and bulk helium ((c)–(d), red) plasmas, from the global simulations in the fixed Φ scan.

radial directions overlaid on top of the poloidal flows, for the same case as shown in figures 2(i)–(l). To account for the vastly different length-scales in the $\nabla\theta$ and $\nabla\psi$ direction, the fluxes are normalized to typical pedestal and poloidal lengths, specifically $(\Gamma \cdot \psi/(\Delta r), \Gamma \cdot \theta/(2\pi a))$, where Δr is the pedestal width in meters, a the minor radius on the outboard side and θ and ψ are unit vectors in the $\nabla\theta$ and $\nabla\psi$ direction, respectively.

As seen in the lower panels of figure 6, the dynamics of the local simulations is rather simple: the small radial fluxes are superimposed on weakly varying poloidal fluxes. In contrast, in the global simulations we find a much richer pattern of fluxes, with stagnation points and vortices in the radial-poloidal plane. Sufficiently far from the pedestal region the flows approach their local behavior. The more complex radial flow patterns are not completely localized to the pedestal, but extend a few orbit widths into the core region, which is more visible for the deuterium species.

The vortices in figure 6 depend on the values of radial and poloidal fluxes, and are thus sensitive to the slight shifts in flows observed by changing plasma composition. To only consider the spatial variations of the fluxes, we evaluate the vorticity, defined as

$$\omega = \frac{1}{\bar{n}} \hat{\phi} \cdot \nabla \times \Gamma \sim \frac{1}{\bar{n}} \left(\frac{d\Gamma_p}{dr} - \frac{1}{a} \frac{d\Gamma_r}{d\theta} \right). \quad (18)$$

The vorticities corresponding to figure 2 are displayed in figure 7. Just like the flows, the vorticities are largely unaffected by exchanging bulk and impurity species, and both helium and deuterium display similar structures. In particular, both species display ‘V’-like arms of high vorticity in the pedestal. The apparent differences between the He and D flows in figure 2 may be due to constant flows that mask the radial and poloidal variations, which are more sensitive to global physics. Similarly, sloped vorticity structures extend from the pedestal into the core, and reveal global effects reaching far into the core. It is interesting to note that the slope of the arms is different between the different species, so that the helium vorticity structure extends over all poloidal angles within the width of the pedestal. This behavior is

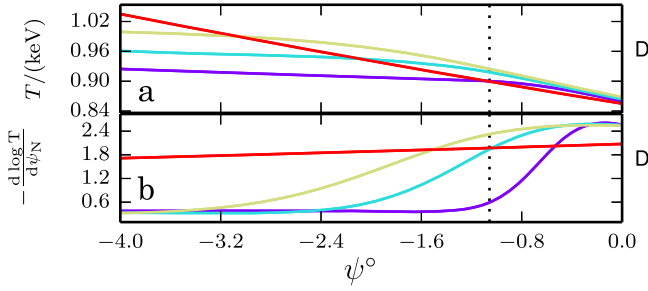


Figure 8. Temperature (a) and logarithmic temperature gradient (b) profiles in the transition-length scan. Violet: baseline temperature profile in figure 1; cyan, a transition length doubled; yellow, transition length tripled; red, no transition in temperature gradients.

consistent with helium flows approaching their local values sooner due to their smaller orbit width.

The divergence of the radial fluxes is strongly affected by a radial variation in the diamagnetic flux, and thus it is expected that radially global flow effects are localized to regions where the density or the driving gradients abruptly change. For our model profiles, the density drops inside the pedestal, and the ion temperature gradient rapidly increases at the pedestal top (as expected in a real pedestal). In order to demonstrate the effect of the location of changes in diamagnetic flow strength, we modify our ion temperature profiles. In a scan, we increase the radial length scale over which the logarithmic temperature gradient transitions from its core value to its pedestal value; see the corresponding temperature profiles and logarithmic gradients in figure 8 (transition length scale increases from violet to yellow).

Increasing the transition region has a twofold effect: the transition becomes less abrupt, and the effective location where the transition happens moves further outside the pedestal. As a result, the radially global effects in the flow structure become weaker and start to extend further away from the pedestal, as illustrated in figure 9. We also consider a temperature profile with no transition region (red curve) in figures 8, and 9(g) and (h). This shows much weaker, but still visible, deviations from the local simulation in terms of flow patterns. However we have to interpret the ‘no-transition’ results carefully, since in this case the sources were non-negligible even close to the radial boundaries. Nevertheless, it also underlines the importance of the changes in the ion temperature gradient in driving unexpected poloidal flow patterns.

Finally, we consider the poloidal structure of the poloidal flows in the middle of our pedestal region for the various temperature profiles of figure 8. The poloidal flow coefficients at $\psi^\circ = -0.563$ are shown in figure 10 with the same color coding. For the baseline case (violet line) there are substantial poloidal variations of k_p for both ion species, being higher (or more positive) on the HFS, and lower (more negative) on the LFS. The variation is not sinusoidal, and the local maxima and minima (several of them) appear at poloidal locations away from the mid-plane. With increasing transition length (cyan and yellow curves), the poloidal variation becomes milder, while the minima move to the outboard mid-plane and

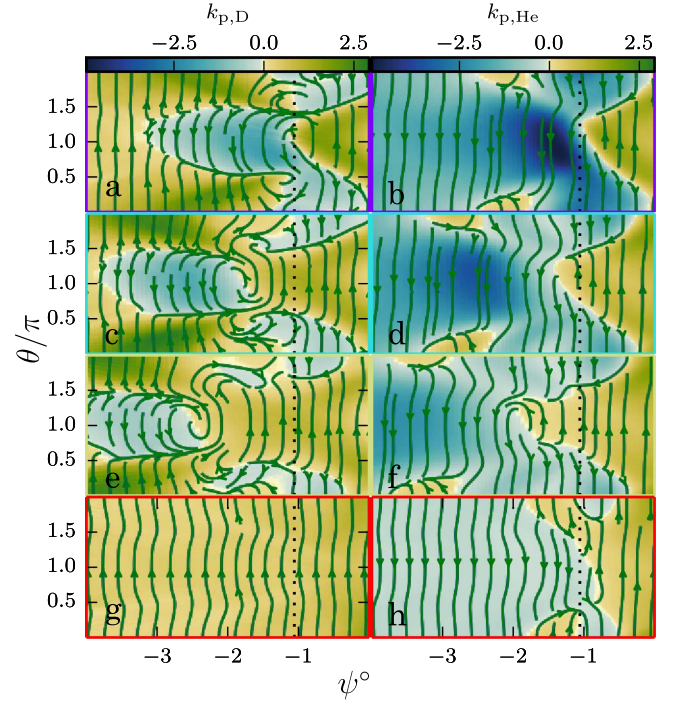


Figure 9. Foreground: stream-plot of the deuterium and helium fluxes in the radial-poloidal plane. Background: k_p . (a)–(b): baseline temperature profile in figures 1; (c)–(d): transition length doubled; (e)–(f): transition length tripled; (g)–(h): no transition. D (a), (c), (e), (g) and He (b), (d), (f), (h) ion species in a deuterium bulk plasma.

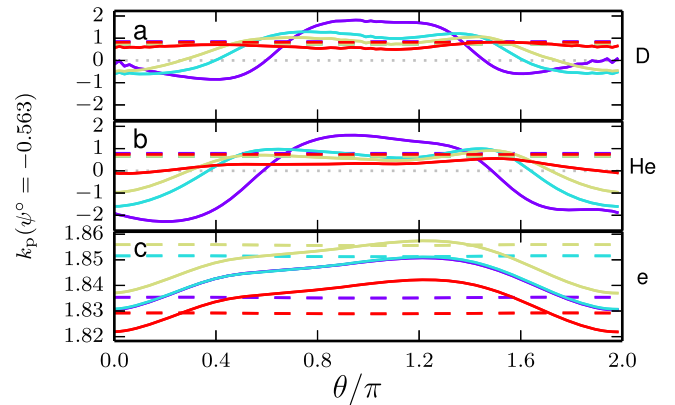


Figure 10. The k_p corresponding to figures 9(a), (c), (e) and (g) (blue, cyan, green, and red curves, respectively), in the middle of the pedestal ($\psi^\circ = -0.563$) for local (dashed lines) and global (solid) simulations.

merge, and the maxima move towards the upper and lower parts of the flux surface. In the no-transition case (red curve), the poloidal variation is weak, but still present, and the global value of k_p is lower than the local one. For electrons (figure 10(c)), the poloidal flows essentially remain local (note the magnified y-axis scale).

3.2. Fixed Φ radial flows and fluxes

To get a clearer picture of the effects of helium concentration on transport, we calculate the total radial particle, conductive heat and toroidal momentum fluxes in the fixed Φ scan. These are displayed in figure 11, normalized by the core species

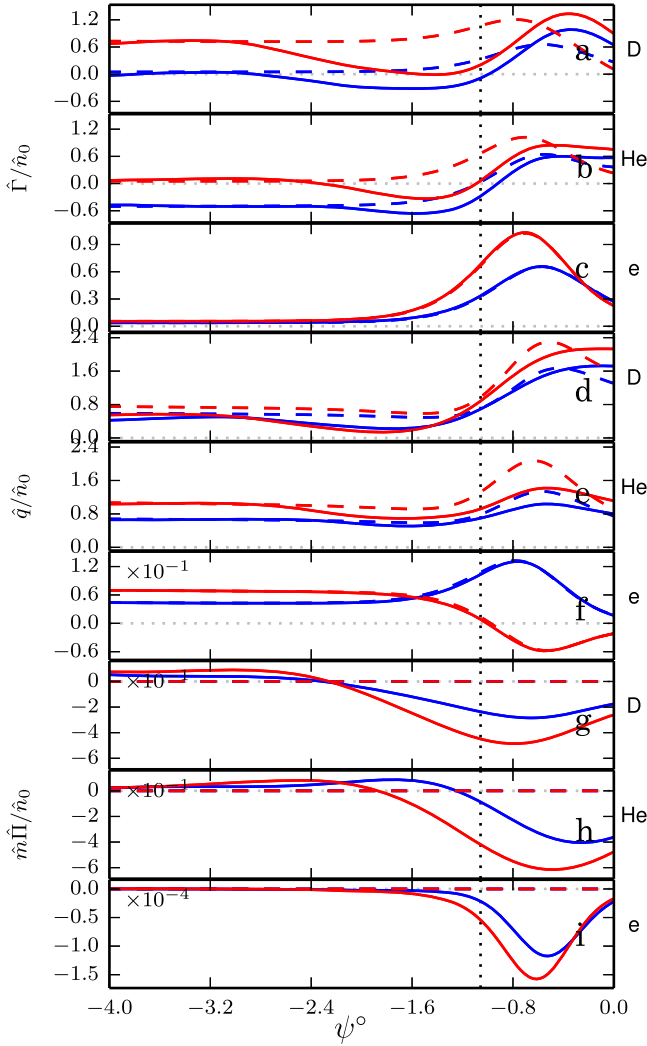


Figure 11. Particle (a)–(c), heat (d)–(f) and momentum (g)–(i) fluxes for bulk D (blue curves) and He (red) plasmas in the fixed Φ scan. Solid (dashed) lines are global (local) results.

density \hat{n}_0 to assist the comparison of the trace and non-trace scenarios.

From figure 11, we can make a few general observations. Firstly, the electron fluxes are practically local by virtue of their small orbit width and large flows, so the electron global and local curves almost overlap (except for the momentum flux figure 11(i), which has no physical relevance as it is small in the electron-to-ion mass ratio—we show it nevertheless for completeness). Since electrons are often omitted from neo-classical simulations, it deserves mention that they can develop a substantial particle flux inside the pedestal. This is the result of the large electron temperature gradient, and it is also present in local simulations.

Secondly, as seen in figures 11(a), (b), (d) and (e), the global ion fluxes in the near-pedestal core tend to be reduced compared to the corresponding local fluxes. Modifications to the ion heat flux compared to the conventional local theory have been predicted by analytical models [32–35] retaining the $\mathbf{v}_E \cdot \nabla g$ term, however in our simulations the radial coupling from the $\mathbf{v}_m \cdot \nabla g$ also plays an important role in

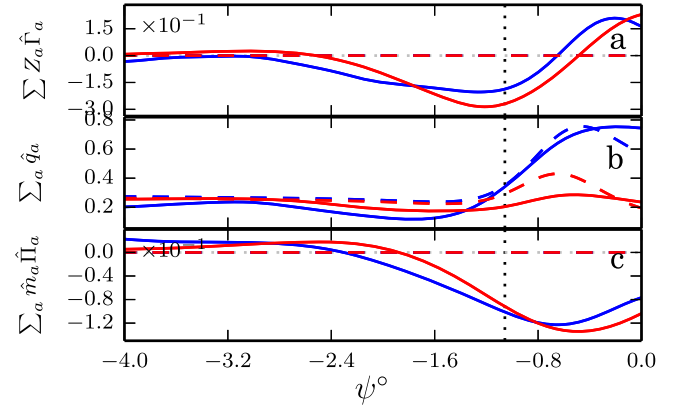


Figure 12. Current (a) and total heat (b) and momentum (c) flux, for bulk D (blue curves) and He (red) plasmas in the fixed Φ scan. Solid (dashed) lines are global (local) results.

setting the radial fluxes. Here, the modifications are especially notable for the particle fluxes figures 11(a) and (b), which change sign compared to the local results in the near-pedestal core. The width of the affected region scales with the orbit width and is thus larger for D than He; accordingly, the fluxes reach local values further away from the pedestal in the D plasma. Such ‘overshoot’ behavior is also seen in the momentum fluxes figures 11(g) and (h), which instead are increased in the near-pedestal core compared to their local value (that is zero).

The flux surface average species-summed toroidal angular momentum balance states that the named quantity changes in time due to a divergence of the radial momentum transport ($\sim d_\psi \sum_a \hat{m}_a \hat{\Pi}_a$), a torque corresponding to any radial currents ($\sim \sum_a Z_a \hat{\Gamma}_a$), or momentum sources. In our *steady state* simulations these three contributions should add up to zero. However, in the calculations presented here there are no momentum sources, thus any momentum transport requires the existence of a radial current. This is indeed the case: figures 12(a) and (c) show the corresponding finite radial currents and toroidal angular momentum transport, respectively. (Recall that we do not enforce the ambipolarity of fluxes, and the radial electric field is not solved for in our simulations—but is an input—while the flows are outputs.) This explains why the particle fluxes are below the local values on one side of the pedestal, and above on the other side: the current must integrate to zero over the entire domain for the momentum transport to approach its local value (i.e. vanish) far from the pedestal. We note that although there are non-intrinsically ambipolar processes in the pedestal which could balance our radial currents (due to orbit losses, ripple fields, etc), the radial current we observe is not a necessary feature, but rather a consequence of not allowing for momentum sources. In appendix C we demonstrate that radial currents can be replaced by momentum sources, and it does not have a significant effect on the flow structures.

From figure 12(c), we see that the total momentum flux has roughly the same peak value in both D and He plasmas, although the shape of the curve is wider in the bulk deuterium simulation, again due to the larger orbit width. We emphasize that the finite momentum transport observed here is purely a

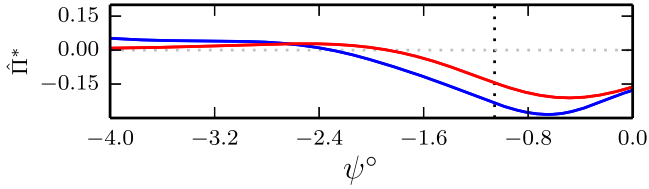


Figure 13. Total momentum flux in figure 12(c) normalized to be a proxy for the effective Prandtl number in the pedestal (19), for the fixed Φ scenario.

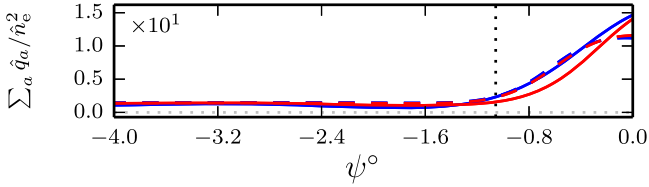


Figure 14. The total heat flux in figure 12(b) divided by \hat{n}_e^2 .

radially global effect. In local theory the momentum transport is a small, higher order quantity. When δ_X is not small for all input profiles X , momentum transport is not small in general. To demonstrate that the magnitude of the momentum transport we observe can be experimentally relevant, we normalize the momentum flux so that it becomes a proxy for the effective Prandtl number in the pedestal [36]

$$\hat{\Pi}^* = \sum_a \hat{m}_a \hat{\Pi}_a \left\{ \frac{\hat{n}_i d_\psi \hat{T}_i}{\hat{q}_i \Delta} \frac{1}{\hat{m}_i d_\psi (\langle \hat{V}_{ti} \rangle \hat{n}_i)} \right\}_{\text{ped}}. \quad (19)$$

The expression with the ‘ped’ subscript is evaluated in the middle of the pedestal ($\psi^\circ = -0.563$), and ‘i’ denotes the bulk ion species⁴. This $\hat{\Pi}^*$ is displayed in figure 13, for the fixed Φ simulations. We find that the effective Prandtl number reaches about 0.35 and 0.24 for D and He bulk plasmas, respectively. This is comparable to experimentally observed effective Prandtl numbers in the plasma core of JET [37] and KSTAR [38]. Since experimental ion heat transport can be comparable to the neoclassical predictions in a pedestal [39], assuming that our results extrapolate to large temperature gradient, we may expect finite orbit width effects to significantly contribute to the total momentum transport in a pedestal⁵.

Next we consider bulk species effects on the total neoclassical conductive heat flux, shown in figure 12(b). Its peak value is reduced by a factor 4 when going from a deuterium to a helium plasma. This is consistent with the $q \propto n_e^2$ scaling from the local banana-regime analysis [31], and compensating for this scaling yields figure 14, where the different simulations have similar peak values.

We also observe that the helium heat flux is lowered compared to local predictions (figure 11(e)), whereas the deuterium heat flux is comparable to the local values (figure 11(d)). This is due to the fact that the orderings (7)

make the helium density pedestal sharper than the deuterium density pedestal, which results in a lower n_{He} further out in the pedestal, and thus a reduced heat flux, from $\hat{q} \propto \hat{n}^2$. Since the ion heat fluxes in the global simulations peak further out compared to the local simulations (figures 11(d) and (e)), the global peak values of \hat{q} are also affected by the reduced n_{He} in the buffer region, which may be a contributing factor to the reduction of the global q_{He} compared to the local value.

4. Conclusions

We have studied finite orbit width effects on the neoclassical toroidal and poloidal flows and cross field fluxes, in density pedestals of deuterium–helium mixture plasmas. In a radially global treatment we allow for ion orbit width scale radial density variations and strong radial electric fields, as long as the ions are electrostatically confined and are characterized by subsonic flow speeds. The deuterium–helium ratio scans were performed keeping either the electrostatic potential variation or the electron density profile fixed, leading to surprisingly similar results.

The perturbed neoclassical distribution is modified compared to the radially local treatment, since magnetic and $E \times B$ drift contributions to the advection of the perturbed distribution need to be retained. In addition, non-standard terms appear in the expressions for the flows, corresponding to an $E \times B$ advection of poloidal density perturbations and, more importantly, to the radial variation of diamagnetic fluxes. The resulting poloidal flows exhibit complex radial–poloidal features which vary on a small radial scale, including poloidal sign changes of the poloidal flow. The main reason is that the poloidally local radial particle fluxes are not divergence free in isolation due to the sharp profile variations, which require poloidal return flows to make the total fluxes divergence free. Such flow structures are found to be sensitive to abrupt radial variations in the ion temperature gradient, and can extend quite far into the core if the ion temperature gradient transitions between its core and pedestal value on a long radial scale.

The near-pedestal core values of the global neoclassical particle and conductive ion heat fluxes are often reduced compared to the local results, as a result of an overshoot of decreased fluxes away from the pedestal. Inside the pedestal the heat fluxes are mostly reduced compared to their local values.

We observe a finite radial current, which at least partially arises as no momentum sources were included in these simulations. However it can also represent a physically meaningful charge separation process due to finite orbit width effects, which in steady state needs to be compensated by other non-intrinsically ambipolar processes. The effects of replacing radial current with momentum sources is the subject of ongoing investigation.

The sizable neoclassical toroidal angular momentum transport we observe only appears in global theory. The momentum flux, when normalized to represent an effective Prandtl number, takes on values (few tens of percent)

⁴ Note that [36] defines the momentum flux in terms of mv_t , with v_t being the toroidal velocity, while we use toroidal angular momentum over mass Rv_t .

⁵ Charge-exchanging neutrals coupled to the neoclassical ion distribution is another mechanism where collisional physics is relevant to the momentum transport in the edge [40, 41].

comparable to experimental values of the effective Prandtl number observed in the plasma core. This is a potentially important observation since the heat fluxes in the pedestal can be dominated by the neoclassical ion heat flux. This implies that if our results extrapolate to large ion temperature gradients (where a full- f treatment is unavoidable), radially global effects might account for a significant fraction of the momentum transport in the inner region of the pedestal.

Acknowledgments

The authors are indebted M Landreman for support with the PERFECT code and for enlightening discussions. The authors are also grateful to T Fülöp and E Highcock for discussions and instructive comments on the manuscript. IP and SB were supported by the International Career Grant of Vetenskapsrådet (VR) (Dnr. 330-2014-6313) and Marie Skłodowska Curie Actions, Cofund, Project INCA 600398. JO and SN were funded by the Framework Grant for Strategic Energy Research of VR (Dnr. 2014-5392). The simulations used computational resources of Hebbe at C3SE (project nr. C3SE2016-1-10 & SNIC2016-1-161) and the ARCHER UK National Supercomputing Service.

Appendix A. Model pedestal profiles and magnetic geometry

Due to the constraints on the T and η profiles (7), we use simple model profiles for our simulations.

Specifically, an mtanh transition between two constant gradient regions is implemented as

$$X = \frac{X_{\text{ped}} + X_{\text{SOL}} + (a - b)w_{\text{ped}}/2}{2} - \frac{X_{\text{ped}} - X_{\text{SOL}} + (a + b)w_{\text{ped}}/2}{2} \tanh(r) + \frac{a(\psi - \psi_0)e^{-r} + b(\psi - \psi_0)e^r}{e^{-r} + e^r}, \quad (\text{A1})$$

where X is a generic profile, $r = \frac{(\psi - \psi_0)}{w_{\text{ped}}/2}$, w_{ped} is the pedestal width, a (b) the core (SOL) asymptotic profile gradients; ψ_0 is the position of the middle of the pedestal. Here ‘SOL’ represents the numerical buffer region outside $\psi^0 = 0$.

The magnetic field is assumed not to vary notably over the pedestal region, and we thus use a radially constant, local Miller geometry [30] with parameters: $\kappa = 1.58$, $s_\kappa \equiv (r/\kappa)d\kappa/dr = 0.479$, $\partial R/\partial r = -0.14$, $\delta = 0.24$, $s_\delta \equiv (r/\sqrt{1 - \delta^2})d\delta/dr = 0.845$, $q = 3.5$, $\epsilon \equiv r/R = 0.263$, where κ is the elongation, δ the triangularity and the corresponding s_X parameters measure their shear.

Appendix B. Insensitivity to boundary conditions

Based on the size of the global term in the DKE (8)—which sets the radial coupling—the radial correlations are expected

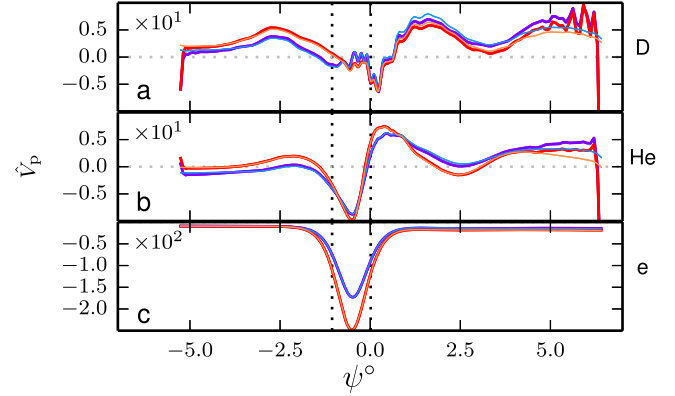


Figure 15. Global outboard poloidal flows in a fixed Φ scan with Dirichlet (thick) and Neumann (thin) boundary conditions.

to decrease outside the pedestal region. As a consequence, the flows and fluxes in the pedestal are essentially decorrelated from the boundary conditions, provided that the boundaries are sufficiently far away from the pedestal.

To demonstrate this, we performed identical simulations with Neumann boundary conditions ($v_{\text{d0}} \cdot \nabla g = 0$) instead of Dirichlet ($g = g_{\text{local}}$). The resulting poloidal flows are displayed in thin lines figure 15 and largely overlap around the pedestal with the Dirichlet results indicated with thick lines—even though the Dirichlet boundary condition can introduce massive oscillations near the boundaries.

The poloidal flows were chosen for this test as they are particularly sensitive to numerical errors, since their evaluation involves a derivative of simulation outputs (the final term in (15)). Similar or higher degrees of agreement are also found for the poloidal variation of V_p in the middle of the pedestal, and other quantities such as the radial fluxes and sources. Thus, we concluded that the results indeed are largely independent of the boundary conditions.

Appendix C. Radial current replaced by momentum sources

We observe a finite radial current in our simulations, which is balanced by non-quasineutral particle sources. If this would be the only radial current, the corresponding time evolution of the electric field would be inconsistent with the assumption of steady state. Even though it cannot be ruled out that other, not modeled, non-intrinsically ambipolar processes cancel our radial current, the appearance of a radial current in the simulation may nevertheless be concerning. Note however, that since we do not solve for the radial electric field our current is not a source of any numerical inconsistency in the simulation.

The torque from the radial current appears in the species-summed toroidal angular momentum equation, and in steady state it is balanced by the divergence of the toroidal angular momentum flux, and momentum sources, if any. In the simulations presented here no momentum sources were considered, therefore it is possible that the current we observe develops merely to balance the radial variation of the

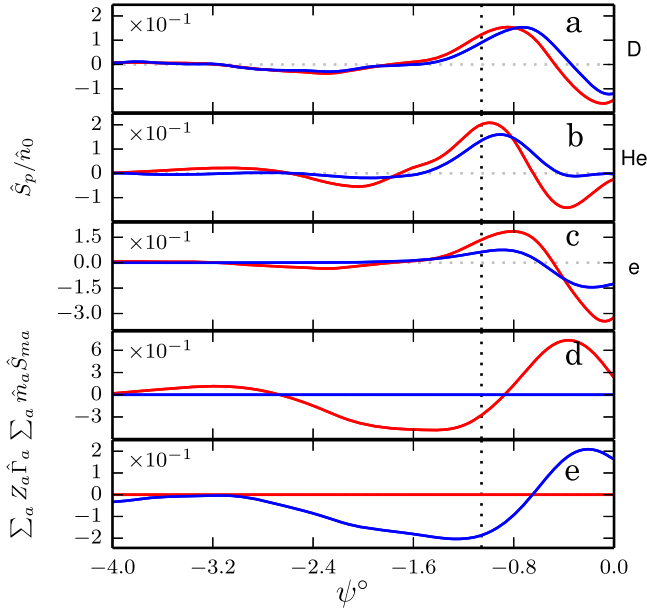


Figure 16. Comparison of particle (a)–(c) and total momentum (d) sources, and radial current (e), between our baseline case (blue curves) and the case where the radial current is required to vanish (red curves).

momentum flux, and that a radial current may not be necessary if we allow for momentum sources. Here we show results indicating that this is the case, although a thorough investigation of the problem is outside the scope of this paper.

Momentum sources can arise from numerous effects, a few candidates near the edge are: the radial variation of turbulent momentum fluxes, atomic physics processes [41], or orbit loss effects [42]. However, we will not dwell on the physical origin of the momentum sources, but instead solve for the radial dependence of a momentum source profile by requiring the radial current to vanish, $\sum_a Z_a \hat{\Gamma}_a = 0$. This requirement represents only one additional constraint per radial grid point (in contrast to one for each species), and accordingly, it allows us to solve for only one new radial profile. To eliminate the corresponding degrees of freedom we assumed momentum sources for the various species to be proportional to the mass and the concentration of the species in the core, $\hat{S}_{ma} \propto m_a n_{0a} \hat{S}_m$, and we solve only for \hat{S}_m . The velocity space structure of the momentum sources was taken so that they do not contribute to parallel heat fluxes, and we assume the sources to be poloidally uniform. These choices are not motivated by any particular physical process, but should be sufficient for our purposes.

Using the baseline deuterium bulk plasma case, we performed a simulation where we allowed for momentum sources by the scheme specified above. In figure 16 we show particle and momentum sources for the simulation with zero radial current (red curves) and compare it to the results without momentum sources (blue curves). As clearly seen in figure 16(e), it is possible to enforce a vanishing radial current (red curve is zero), but in that case there is a need for finite momentum sources (see red curve in figure 16(d)). The particle sources, shown in figures 16(a)–(c), have changed to

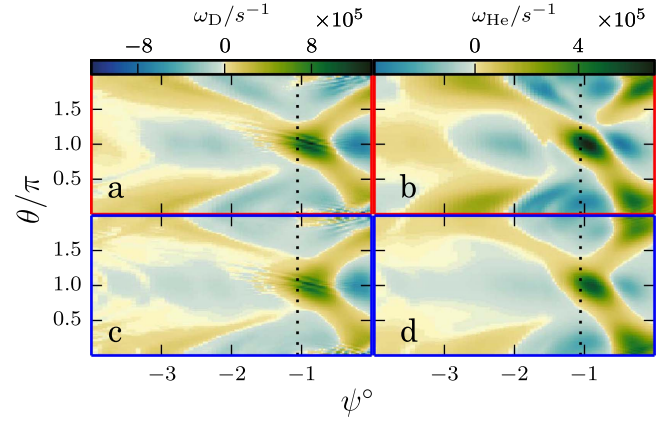


Figure 17. Vorticities of flows in the radial–poloidal plane for the baseline bulk deuterium plasma with (a), (b) and without (c), (d) momentum sources for the D (a), (c) and He (b), (d) species.

achieve a zero net charge source. They still share qualitative similarities with those in the simulation without momentum sources: in both cases the particle sources have a positive peak a little inside the pedestal top and drop towards the separatrix in such a way that they change sign around the middle of the model pedestal.

Importantly, the interaction of the radial and poloidal fluxes and the corresponding complex flow patterns are not very sensitive to the replacement of radial currents with momentum sources in the simulation. This is perhaps best illustrated by comparing vorticities, see figure 17, where (a) and (b) shows results with zero radial current, and the case without momentum sources is shown in (c) and (d).

While the issue deserves a more detailed study, here we have demonstrated that radial currents are not a necessary feature of our simulations, and that from the point of view of flows it is of secondary importance whether the radial variation of the toroidal angular momentum is balanced by a torque from a radial current or by momentum sources. The red curve of figure 16(d) and the blue curve of (e) are proportional to the radial variation of the total toroidal angular momentum flux in their respective cases (\hat{S}_{ma} is here defined to make the proportionality constant the same in both cases). Their similarity suggests that the momentum fluxes are similar in the two cases. Without adding a corresponding figure we note that this is indeed the case, although the magnitude of the momentum transport is somewhat higher in the zero radial current case, as expected from comparing the magnitudes in figures 16(d) and (e).

References

- [1] Wagner F *et al* 1984 Development of an edge transport barrier at the H-mode transition of ASDEX *Phys. Rev. Lett.* **53** 1453–6
- [2] Biglari H, Diamond P H and Terry P W 1990 Influence of sheared poloidal rotation on edge turbulence *Phys. Fluids B* **2** 1–4

- [3] Staebler G and Dominguez R 1991 Electric field effects on ion temperature gradient modes in a sheared slab *Nucl. Fusion* **31** 1891–8
- [4] Haye R L, Osborne T, Rettig C, Greenfield C, Hyatt A and Scoville J 1995 Core flow shear as the cause of very high confinement in the DIII-D tokamak *Nucl. Fusion* **35** 988
- [5] Burrell K H 1997 Effects of $E \times B$ velocity shear and magnetic shear on turbulence and transport in magnetic confinement devices *Phys. Plasmas* **4** 1499–518
- [6] Highcock E G, Barnes M, Parra F I, Schekochihin A A, Roach C M and Cowley S C 2011 Transport bifurcation induced by sheared toroidal flow in tokamak plasmas *Phys. Plasmas* **18** 102304
- [7] Sauter P, Pütterich T, Ryter F, Viezzer E, Wolfrum E, Conway G, Fischer R, Kurzan B, McDermott R, Rathgeber S and the ASDEX Upgrade Team 2012 L- to H-mode transitions at low density in ASDEX Upgrade *Nucl. Fusion* **52** 012001
- [8] Haskey S R, Grierson B A, Burrell K H, Chrystal C, Groebner R J, Kaplan D H, Pablant N A and Stagner L 2016 Measurement of deuterium density profiles in the H-mode steep gradient region using charge exchange recombination spectroscopy on DIII-D *Rev. Sci. Instrum.* **87** 11
- [9] Silburn S A, Harrison J R, Howard J, Gibson K J, Meyer H, Michael C A and Sharples R M 2014 Coherence imaging of scrape-off-layer and divertor impurity flows in the mega Amp spherical tokamak *Rev. Sci. Instrum.* **85** 11
- [10] Churchill R M *et al* (Alcator C-Mod Team) 2015 Poloidal asymmetries in edge transport barriers *Phys. Plasmas* **22** 056104
- [11] Menmuir S, Giroud C, Biewer T M, Coffey I H, Delabie E, Hawkes N C, Sertoli M and J E Contributors 2014 Carbon charge exchange analysis in the ITER-like wall environment *Rev. Sci. Instrum.* **85** 11
- [12] Kim J, Burrell K H, Gohil P, Groebner R J, Kim Y-B, John H E St, Seraydarian R P and Wade M R 1994 Rotation characteristics of main ions and impurity ions in H-mode tokamak plasma *Phys. Rev. Lett.* **72** 2199–202
- [13] Wolfrum E *et al* (the ASDEX Upgrade Team) 2015 Overview of recent pedestal studies at ASDEX Upgrade *Nucl. Fusion* **55** 053017
- [14] Kim Y B, Diamond P H and Groebner R J 1991 Neoclassical poloidal and toroidal rotation in tokamaks *Phys. Fluids B* **3** 2050–60
- [15] Testa D, Giroud C, Fasoli A, Zastrow K-D and EFDA-JET Team 2002 On the measurement of toroidal rotation for the impurity and the main ion species on the Joint European Torus *Phys. Plasmas* **9** 243–50
- [16] Landreman M and Ernst D R 2012 Local and global Fokker–Planck neoclassical calculations showing flow and bootstrap current modification in a pedestal *Plasma Phys. Control. Fusion* **54** 115006
- [17] Landreman M, Parra F I, Catto P J, Ernst D R and Pusztai I 2014 Radially global δf computation of neoclassical phenomena in a tokamak pedestal *Plasma Phys. Control. Fusion* **56** 045005
- [18] Pusztai I, Buller S and Landreman M 2016 Global effects on neoclassical transport in the pedestal with impurities *Plasma Phys. Control. Fusion* **58** 085001
- [19] Maggi C *et al* 2015 Pedestal confinement and stability in JET-ILW ELMy H-modes *Nucl. Fusion* **55** 113031
- [20] Pütterich T, Viezzer E, Dux R, McDermott R and the ASDEX Upgrade Team 2012 Poloidal asymmetry of parallel rotation measured in ASDEX Upgrade *Nucl. Fusion* **52** 083013
- [21] Fülöp T and Helander P 1999 Nonlinear neoclassical transport in a rotating impure plasma with large gradients *Phys. Plasmas* **6** 3066–75
- [22] Fülöp T and Helander P 2001 Nonlinear neoclassical transport in toroidal edge plasmas *Phys. Plasmas* **8** 3305–13
- [23] Landreman M, Fülöp T and Guszejnov D 2011 Impurity flows and plateau-regime poloidal density variation in a tokamak pedestal *Phys. Plasmas* **18** 092507
- [24] Churchill R M *et al* (Alcator C-Mod Team) 2015 Poloidal asymmetries in edge transport barriers *Phys. Plasmas* **22** 056104
- [25] Pusztai I, Landreman M, Mollén A, Kazakov Y O and Fülöp T 2014 Radio frequency induced and neoclassical asymmetries and their effects on turbulent impurity transport in a tokamak *Contrib. Plasma Phys.* **54** 534–42
- [26] SFINCS user manual, (2016) <https://github.com/landreman/sfincs/blob/master/doc/manual/version3/SFINCSUserManual.pdf> (Accessed: 21 March 2017)
- [27] Landreman M, Smith H M, Mollén A and Helander P 2014 Comparison of particle trajectories and collision operators for collisional transport in nonaxisymmetric plasmas *Phys. Plasmas* **21** 042503
- [28] Pusztai I, Candy J and Gohil P 2011 Isotope mass and charge effects in tokamak plasmas *Phys. Plasmas* **18** 122501
- [29] Bessenrodt-Weberpals M *et al* 1993 The isotope effect in ASDEX *Nucl. Fusion* **33** 1205
- [30] Miller R L, Chu M S, Greene J M, Lin-Liu Y R and Waltz R E 1998 Noncircular, finite aspect ratio, local equilibrium model *Phys. Plasmas* **5** 973–8
- [31] Helander P and Sigmar D 2005 Collisional transport in magnetized plasmas *Cambridge Monographs on Plasma Physics* (Cambridge: Cambridge University Press)
- [32] Kagan G and Catto P J 2008 Arbitrary poloidal gyroradius effects in tokamak pedestals and transport barriers *Plasma Phys. Control. Fusion* **50** 085010
- [33] Pusztai I and Catto P J 2010 Neoclassical plateau regime transport in a tokamak pedestal *Plasma Phys. Control. Fusion* **52** 075016
- [34] Catto P J, Kagan G, Landreman M and Pusztai I 2011 A unified treatment of kinetic effects in a tokamak pedestal *Plasma Phys. Control. Fusion* **53** 054004
- [35] Catto P J, Parra F I, Kagan G, Parker J B, Pusztai I and Landreman M 2013 Kinetic effects on a tokamak pedestal ion flow, ion heat transport and bootstrap current *Plasma Phys. Control. Fusion* **55** 045009
- [36] Tala T *et al* (J Contributors) 2007 Toroidal and poloidal momentum transport studies in tokamaks *Plasma Phys. Control. Fusion* **49** B291
- [37] Tala T *et al* 2009 Evidence of inward toroidal momentum convection in the jet tokamak *Phys. Rev. Lett.* **102** 075001
- [38] Ko S H, Kwon J M, Ko W H, Kim S S, Jhang H and Terzolo L 2016 Characteristics of toroidal rotation and ion temperature pedestals between ELM bursts in KSTAR H-mode plasmas *Phys. Plasmas* **23** 062502
- [39] Viezzer E *et al* (the ASDEX Upgrade Team), and (the EUROfusion MST1 Team) 2017 Investigation of inter-ELM ion heat transport in the H-mode pedestal of ASDEX Upgrade plasmas *Nucl. Fusion* **57** 022020
- [40] Fülöp T, Helander P and Catto P J 2002 Effect of poloidal density variation of neutral atoms on the tokamak edge *Phys. Rev. Lett.* **89** 225003
- [41] Omotani J, Pusztai I, Newton S and Fülöp T 2016 Plasma rotation from momentum transport by neutrals in tokamaks *Nucl. Fusion* **56** 124002
- [42] Stoltzfus-Dueck T 2012 Transport-driven toroidal rotation in the tokamak edge *Phys. Rev. Lett.* **108** 065002